Theta oscillons in behaving rats

M. S. Zobaer[1], N. Lotfi[1], C. M. Domenico[2], C. Hoffman[1], L. Perotti[3], D. Ji[2], Y. Dabaghian[1*]

[1]*Department of Neurology,*
The University of Texas Health Science Center at Houston, Houston, TX 77030
[2]*Department of Neuroscience,*
Baylor College of Medicine, Houston, TX 77030,
[3]*Department of Physics, Texas Southern University,*
3100 Cleburne Ave., Houston, Texas 77004,
[*]*e-mail: yuri.a.dabaghian@uth.tmc.edu*

(Dated: April 21, 2024)

Recently discovered constituents of the brain waves—the *oscillons*—provide high-resolution representation of the extracellular field dynamics. Here we study the most robust, highest-amplitude oscillons that manifest in actively behaving rats and generally correspond to the traditional θ-waves. We show that the resemblances between θ-oscillons and the conventional θ-waves apply to the ballpark characteristics—mean frequencies, amplitudes, and bandwidths. In addition, both hippocampal and cortical oscillons exhibit a number of intricate, behavior-attuned, transient properties that suggest a new vantage point for understanding the θ-rhythms' structure, origins and functions. We demonstrate that oscillons are frequency-modulated waves, with speed-controlled parameters, embedded into a noise background. We also use a basic model of neuronal synchronization to contextualize and to interpret the observed phenomena. In particular, we argue that the synchronicity level in physiological networks is fairly weak and modulated by the animal's locomotion.

I. INTRODUCTION

Synchronized neural activity induces rhythmically oscillating electrical fields that modulate circuit dynamics at multiple spatiotemporal scales [1–3]. The corresponding local field potentials (LFPs) are easily recorded and widely used for describing varieties of neurophysiological phenomena [4, 5]. However, our perspective on the LFPs' structure and properties, as well as our interpretation of its functions depend inherently on the techniques used in data analyses. Currently, most studies are based on Fourier paradigm, in which the oscillating LFPs are viewed as a superpositions of harmonics with constant frequencies [6, 7]. The familiar θ, γ, and other "brain waves" are combinations of such harmonics, occupying a particular frequency band [2, 3] (Fig. 1A).

Despite their commonality, Fourier decompositions are known to provide a limited detalization of LFP dynamics, particularly for transient, irregular or noisy data, and thus may obscure the brain wave design. A recently proposed alternative, the *Discrete Padé Transform*[1] (DPT), allows replacing the packets of Fourier harmonics with solitary waves that adapt their frequencies to the fields' ongoing structure [8–10] (Fig. 1B). As it turns out, there are two kinds of such "flexible" frequencies: those that change over time in a regular manner, leaving distinct, contiguous traces on the spectrogram, and those that assume sporadic values from moment to moment. Mathematically, the "irregular" harmonics represent the noise, $\xi(t)$, whereas the "regular" frequencies define the signal's oscillatory part [11, 12] (Fig. 1C, Sec. VI B).

At high temporal resolutions, the "timelines" of regular frequencies produce undulant patterns—the *spectral waves* (Fig. 1C). These waves vacillate around their respective lento-changing means, and span over the frequency domains attributed to the traditional, Fourier-defined rhythms. For example, the lowest-frequency spectral wave, prominent during active behavior, occupies the range that roughly corresponds to the traditional θ-domain [13–17]. The following spectral wave occupies the slow-γ domain [18], and so forth (Fig. 1C). The gap between the mean frequencies is typically larger than the undulations' magnitudes, which allows keeping the standard nomenclature, e.g., using the notation $\nu_\theta(t)$ for the θ-domain spectral wave, $\nu_{\gamma_s}(t)$ for the slow-γ spectral wave, etc. Each contiguous frequency, $\nu_q(t)$, contributes with a certain amplitude, $A_q(t)$, and a phase, $\phi_q(t)$, giving rise to a compound wave,

$$\vartheta_q(t) = A_q e^{i\phi_q(t)}, \tag{1}$$

which we refer to as *brain wave oscillon*, or just *oscillon* for short [11, 12] (Fig. 1B, Sec. VI B). The superposition of the oscillons and the noise, $\xi(t)$, amounts to the original LFP,

$$\ell(t) = A_\theta e^{i\phi_\theta(t)} + A_{\gamma_s} e^{i\phi_{\gamma_s}(t)} + \ldots + \xi(t). \tag{2}$$

Typically, the main contribution is made by the θ-oscillon, then the next biggest contribution comes from the slow-γ oscillon, etc. (Fig. 1D).

Importantly, all oscillon parameters are obtained empirically from the recorded data: the amplitudes, the shapes of the spectral waves and the noise exhibit robust, tractable characteristics that reflect physical organization of the synchronized neuronal activity [19–23]. In other words, the elements of the decomposition (2) can be interpreted not only as structural motifs, but also as functional units within the LFP waves. This raises many questions: what are the physiological properties of the oscillons? Which of their features were previously captured through Fourier analyses, and how accurately? Do the oscillons reveal any new operational aspects of the brain waves?

[1] Throughout the text, terminological definitions are given in *italics*.

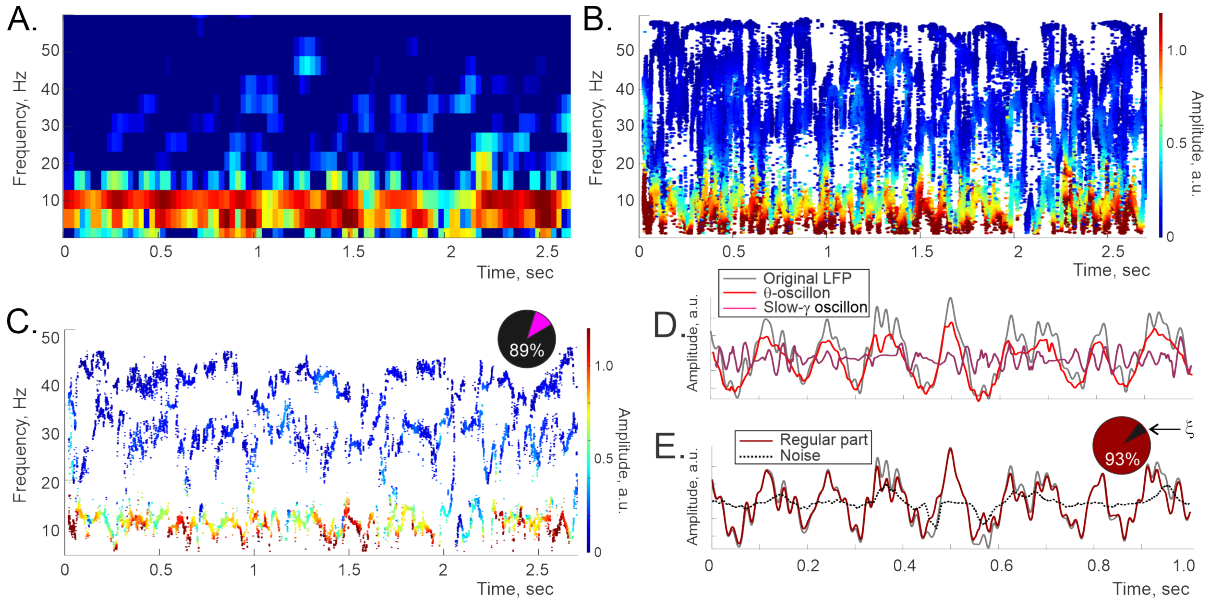

FIG. 1. **Oscillons and spectral waves** constructed for the LFP data recorded in the rat's cortex. **A**. Fourier spectrogram: the high-power stripe between about 4 and 12 Hz marks the conventional θ-band, the slow-γ domain lays approximately between 20 and 45 Hz. **B**. The corresponding full Padé spectrogram, same time resolution, shows the pattern of "flexible" frequencies, both stable and unstable. The vertical position of each dot marks a specific frequency value, the horizontal position marks the corresponding time, and the color indicates the instantaneous amplitude (colorbar on the right). **C**. Most frequencies, (typically over 80%, dark section on the pie diagram), are unstable or "noise-carrying." Removing them reveals the regular Padé spectrogram, on which the stable frequencies trace out regular timelines—*spectral waves*, $\nu_q(t)$. Color change along each spectral wave encodes the corresponding time-dependent amplitude, $A_q(t)$ (Eq. 1). **D**. Combining a particular spectral wave, $\nu_q(t)$, with its amplitude, $A_q(t)$, yields an individual oscillon, as indicated by Equation 1). Shown is a one-second-long segment of the cortical θ-oscillon (red trace) and the slow-γ oscillon (pink trace). Notice that summing just these two oscillons (first two terms in the Eq. 2) already approximates the full LFP profile (gray line) quite closely. **E**. The superposition of all the inputs with regular frequencies (dark red trace), closely matches the amplitude original signal (gray trace). The difference is due to the noise component, $\xi(t)$, carried by the unstable frequencies (dotted black line) typically accounts for less than $5-7\%$ of the signal's net power during active behaviors (dark section on the pie diagram), and about $10-15\%$ during quiescence. Data sampled in a 6 months old, wake male rat during active behavior.

In the following, we focus specifically on the high-amplitude, low-frequency θ-oscillons, recorded in the hippocampal CA1 area and in the cortex of male rats, shuttling between two food wells on a linear track. The experimental specifics are briefly outlined in Section II, (computational techniques and mathematical notions are summarily reviewed in the Supplement, Sec. VI B, for more details see [8–12]). In Section III, we demonstrate that although some qualities of the θ-oscillons parallel those of the traditional (i.e., Fourier-defined) θ-waves, many of their characteristics have not been resolved or even addressed by conventional analyses. In Section IV, we use a basic model of neuronal synchronization to illustrate and contextualize our empirical observations. In Section V, we summarize the results and point out a new vantage point on the information exchange in the hippocampo-cortical network suggested by the newfound architecture of the θ-rhythmicity.

II. METHODS

Experimental procedures. Data was recorded from the CA1 pyramidal cell layer of Long-Evans rats' hippocampus and from anterior cingulate cortex [24]. The animals were trained in a familiar room to run back and forth on a rectangular track for food reward (Fig. 2). The daily recording procedure consisted of two 30 min running sessions. Two diodes were mounted over the animal's head to track its positions, at 33 Hz rate, with a spatial resolution of about 2 mm. Further details on surgery, tetrode recordings and other procedures can be found in [24]. The data analyzed here are not included in [24], but experimental details are identical.

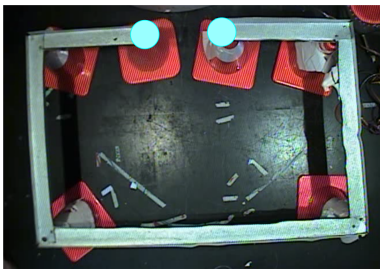

FIG. 2. **Linear track** explored by the rat is 3.5 meters long, a typical run between the food wells (blue dots) takes about 30 sec. Fast moves over the straight segments last 5 – 6 secs, slowdowns occur at the corners and during feeding.

Signal processing. The original LFP data was sampled at S_r = 8 kHz rate, and interpolated to $\tilde{S}_r$ = 36 kHz rate, to improve the quality of the reconstructions at low frequencies. The signals were filtered between 0 and 60 Hz, and downsampled $2 \le m \le 4$ times, producing m nearly identical, interlaced subseries, which helped to ensure robustness and consistency of the results. These and other procedures permitted using high time resolutions ($T_W \approx 50-75$ ms time windows), simultaneously with high frequency resolution of the LFP dynamics (Sec. VI B).

III. RESULTS

The animal's trajectory consisted of intermittent sequence of fast moves along the straight segments of the track, slowdowns at the turning points and the periods when the animal consumed his food reward (Fig. 2). The following analyses target specifically the θ-oscillons' structure during fast moves.

Shape of the oscillons. Similarly to their Fourier counterparts—the traditional hippocampal (f^h_θ) and cortical (f^c_θ) θ-waves—the θ-oscillons, ϑ^h_θ and ϑ^c_θ, increase their amplitudes during active moves (speed s over 2 cm/sec) and diminish (but do not vanish) during slowdowns and quiescence [14–17]. Due to the removed noise, the amplitudes of the hippocampal and cortical θ-oscillons' are lower than the amplitudes of the corresponding Fourier-waves, on average, by 5 – 10%. The *average* frequency span of the hippocampal θ-oscillons is between 3 and 13.5 Hz (mean over 12 four-second-long wave segments), and the cortical θ-oscillons are typically confined between 4 and 12.5 Hz. Although the individual spectral waves' fringes can escape these limits or remain confined within much narrower strips, their spreads generally conform with the traditional θ-bandwidths (Fig. 1A,B).

To put these observations into a perspective, note that there exist several consensual θ-frequency bands, e.g., from 4 to 12 Hz, from 5 to 10 Hz, from 6 to 10 Hz, from 6 to 12 Hz, from 5 to 15 Hz, etc. [25–37]. The shapes of the corresponding Fourier θ-waves differ by about ~ 6%, as measured by the relative amount of local adjustments required to match a pair of waveforms (the Dynamic Time Warping method, DTW [38–40], see Fig. S1). In other words, since bandwidths are obtained through empirically established frequency limits, the resulting wave shapes are fuzzily defined. In contrast, the frequency profiles of the θ-oscillons are determined squarely, over each time interval, by the shapes of their respective spectral waves, which may, at times, drop below 3 Hz, get as high as 20 Hz, or narrow into a tight 1 – 2 Hz band that typically stretches along the mean θ-frequency (Fig. 3A,B).

Overall, the shapes of θ-oscillons are similar to the shapes of the Fourier-defined θ-waves: the DTW-difference between them during active moves are small, $D(\vartheta^h_\theta, f^h_\theta) \approx 6.4 \pm 1.2\%$ and $D(\vartheta^c_\theta, f^c_\theta) \approx 7.1 \pm 1.5\%$ respectively, relative to the waveforms' length. However, adaptively built θ-oscillons capture the ongoing details of the LFP waves better and are hence DTW-closer to the original LFP signal ($D(f^h_\theta, \ell^h) \approx (4 \pm 0.7) D(\vartheta^h_\theta, \ell^h)$, $D(f^c_\theta, \ell^c) \approx (5 \pm 0.9) D(\vartheta^c_\theta, \ell^c)$, values computed for 17 waveforms, for an illustration see Fig. 3B and Fig. S2). Between themselves, the shapes of the hippocampal and the cortical oscillons differ about as much as the traditional, Fourier, θ-waves: over $1-2$ secs segments, $D(\vartheta^h_\theta, \vartheta^c_\theta) \approx D(f^h_\theta, f^c_\theta) \approx 7 \pm 0.8\%$.

Coupling to locomotion. The θ-oscillons' amplitudes and their mean frequencies are coupled to speed, as one would expect based on a host of previous studies of θ-rhythmicity [31–34]. This correspondence is nevertheless informative since oscillons are qualitatively different objects. While the traditional brain waves' frequency is evaluated by tracking their Fourier-envelope (Fig.S3), the oscillons' mean frequency is obtained as their spectral waves' moving mean. As illustrated on Figs. 3C, the two outcomes are consistent, but the latter provides a more nuanced description of the oscillatory trends: both hippocampal and the cortical θ-oscillons' mean frequencies, $\nu^h_{\theta,0}$ and $\nu^c_{\theta,0}$, vary more intricately than their Fourier counterparts, which shows only limited, sluggish changes. Correspondingly, the co-variance of the oscillons' mean frequency with the rat's speed is much more salient (Figs. 3D). Similarities between the two descriptions can be made more conspicuous by scaling the Fourier-frequency up by an order of magnitude (Fig. S4A), which further illustrates that the traditional descriptions capture the mean θ-oscillon dynamics at a diminished scale. Similar mean behavior is exhibited by the slow-γ oscillon also co-varies with speed (Fig. S4B).

Spectral undulations are the oscillons' distinguishing feature that capture detailed aspects of the θ-rhythm's cadence (Fig. 3C). The semi-periodic appearance of the spectral waves suggests that their ups and downs should be decomposable into a harmonics series,

$$\nu_\theta(t) = \nu_{\theta,0} + \nu_{\theta,1} \cos(\Omega_{\theta,1} t + \phi_{\theta,1}) + \nu_{\theta,2} \cos(\Omega_{\theta,2} t + \phi_{\theta,2}) + \dots , \tag{3}$$

where the modulating, embedded frequencies[2], $\Omega_{\theta,i}$, the corresponding modulation depths, $\nu_{\theta,i}$s, and the phases, $\phi_{\theta,i}$ evolve about as slowly as the mean frequency, $\nu_{\theta,0}$ (Fig. 3D). By itself, this assumption is patently generic—given a sufficient number of terms, suitable expansions (3) can be produced, over appropriate time periods, for almost any data series [41]. Question is, whether spectral waves' expansions can be succinct, hold over sufficiently long periods and whether their terms are interpretive in the context of underlying physiological processes.

To test these possibilities, we interpolated the "raw" frequency patterns over uniformly spaced time points and obtained contiguous spectral waves over about 5.5 secs—about 1/6 of a typical trip between the food wells (Fig. 4A). The full wave was then split into 600 ms long, strongly overlapping (by 99.9%) segments, for which we computed power profiles using Welch's method [45, 46], see Sec. VI B. Arranging the results along the discrete time axis yields three-dimensional ($3D$) Welch's spectrograms (*W-spectrograms*), whose lateral sections consist of the familiar instantaneous power-frequency profiles, with peaks marking the embedded frequencies, and whose longitudinal sections show the time dynamics of these peaks (Fig. 4B, see also Fig. S8 in Sec. VI B).

The results demonstrate that both hippocampal and cortical spectral waves have complex dynamics. First, most peaks are localized not only in frequency but also in time: a typical peak grows and wanes off in about $200-300$ ms, i.e., the embedded frequencies and the depth of modulation are highly transitive, changing faster than the mean frequencies by an order of magnitude [12].

[2] The suppression of the "h" and "c" superscripts here and below indicates that a formula or a notation applies to both the hippocampal and the cortical cases.

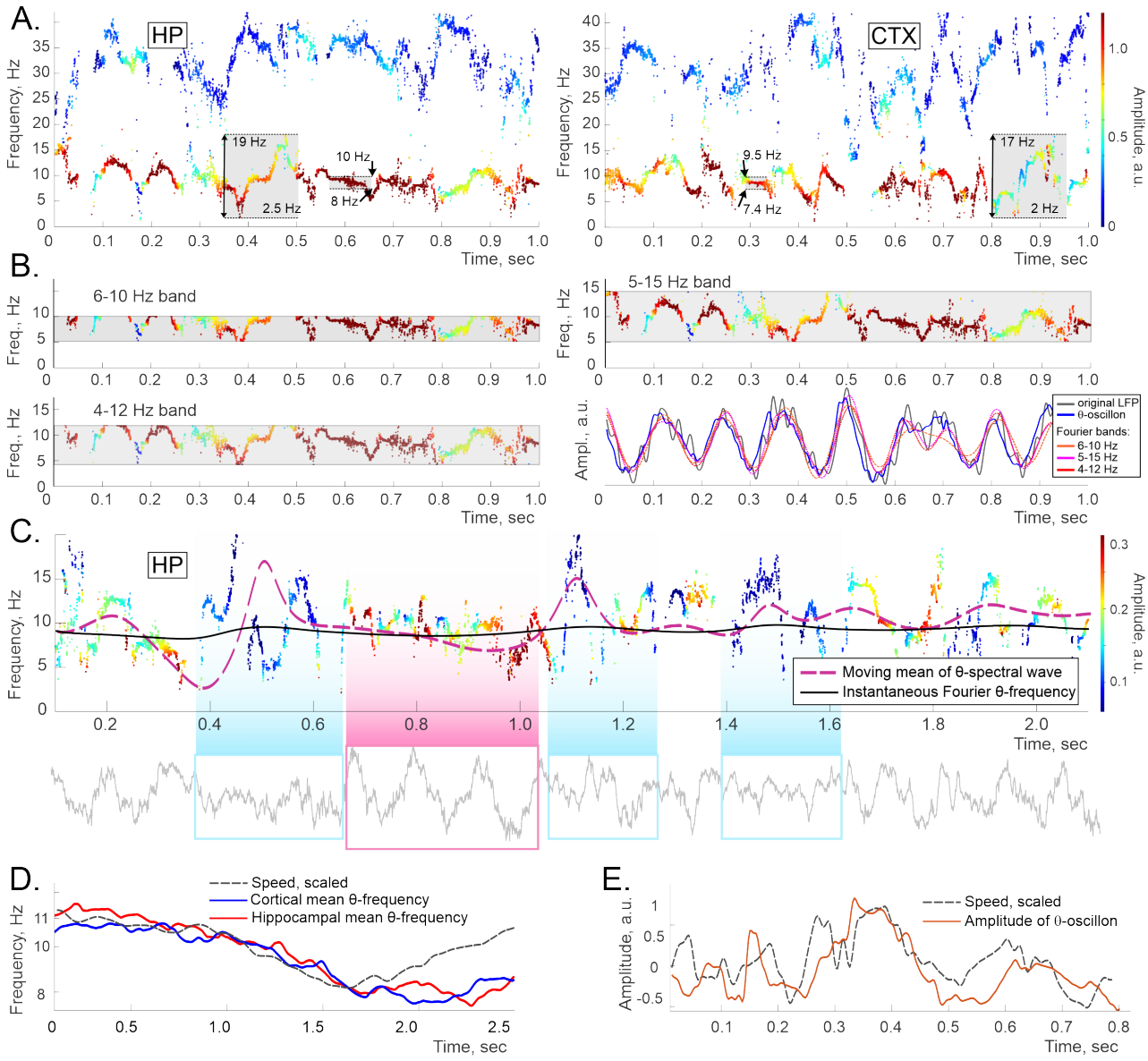

FIG. 3. **A**. The lowest spectral wave occupies the domain that is generally attributed to the θ-frequency band. The color of each dot represents the amplitude, as on Fig. 1. The spectral widths range from about 17 to about 2 Hz (gray boxes). **B**. The hippocampal θ-oscillon's spectral wave, made visible through three "frequency slits" that represent three most commonly used θ-bands, 4-12 Hz, 5-15 Hz, and 6-11 Hz (gray stripes). The frequencies that fit into a slit are the ones that produce the corresponding Fourier wave, shown as red-shaded traces on the bottom right panel. Note that the spectral waves are crosscut by all θ-bands. The Fourier waves are close to each other (DTW distances $D(f^h_{\theta_1}, f^h_{\theta_2}) \approx 6\%$, $D(f^h_{\theta_2}, f^h_{\theta_3}) \approx 5\%$, $D(f^h_{\theta_3}, f^h_{\theta_1}) \approx 8\%$), but further from the θ-oscillon (e.g., $D(\vartheta^h_\theta, f^h_{\theta_2}) \approx 9\%$), which, in turn, is closer to the original LFP (the $\ell(t)$ in Eq. 2, gray trace, $D(\ell^h, \vartheta^h_\theta) = 4\%$). **C**. A longer segment of a hippocampal-θ spectral wave. The nearly-constant solid black trace in the middle shows the instantaneous Fourier θ-frequency. The dashed purple line shows the spectral wave's moving average, which clearly provides a more detailed description of the θ-rhythm's trend. The waveform (bottom panel) is regular when the mean is steady (pink box), and corrugates when the mean is perturbed (blue boxes). **D**. The moving mean of the hippocampal and cortical θ-oscillons' spectral waves (blue and red curves respectively) follow the speed profile (dashed gray curve). The latter was scaled vertically to match, for illustrative purposes, see also Fig. S4. **E**. The amplitude of the hippocampal θ-oscillon also co-varies with the speed, which was captured previously via Fourier analyses [31, 34, 35].

Thus, the representation (3) holds over relatively short periods (typically 1 sec or less, see [11]), and then requires corrections in order to account for rapidly accumulating changes. In other words, the θ-oscillons may be viewed as relatively steady oscillatory processes, altering at the behavioral timescale at around $\sim \nu_{\theta,0} \approx 8$ Hz, and modulated by series of swift, transient vibrations.

Curiously, certain peaks in the W-spectrograms appear and disappear repeatedly near the same location along the Ω-axis, i.e., fast moves can repeatedly incite θ-rhythm's vibrations at the same embedded frequencies (Fig. 4B, Fig. S5), indicating restorative network dynamics [47]. Other peaks appear sporadically, possibly reflecting spontaneously generated oscillations, resonances or brief external contributions (Fig. 4B, [12]). In either case, these events are coupled with the rat's ongoing behavior: power flows into higher embedded frequencies (Ω_i over $4-5$ Hz) as the speed increases, and recedes as the speed drops, i.e., fast moves drive spectral undulations both in the hippocampus and in the cortex. Markedly, cortical responses tend to delay by about $\bar{\tau}^c = 200-300$ ms, while the mean hippocampal delay is shorter, about $\bar{\tau}^h = 70-120$ ms (Fig. 4B). With these shifts taken into account, spectral waves are structurally closer to one another than the corresponding oscillons $D(\nu^h_\theta, \nu^c_\theta) \approx (0.8 \pm 0.12) D(\vartheta^h_\theta, \vartheta^c_\theta)$, which may be viewed as a manifestation of the hippocampo-cortical frequency coupling at the circuit level.

The peak magnitudes associated with the individual embedded spectral frequencies Ω_i (the coefficients of the oscillatory terms in the Equation 2) tend to grow roughly proportionally to speed,

$$\nu_{\theta,i}(t) \approx \alpha_i + w_i \cdot s^{\kappa_i}(t - \tau_i), \tag{4}$$

where the hippocampal and cortical exponents are close to 1 ($\bar{\kappa}^h = 1.2 \pm 0.44$ vs. $\bar{\kappa}^c = 0.9 \pm 0.35$, evaluated for 10 peaks each). The coefficients α_i, w_i and the temporal lags of the peaks' responses, τ_i, vary by about $10-25\%$ from one embedded frequency to another, in both brain areas.

The coupling (4) between the embedded frequency magnitudes and speed is foreseeable: linear modulation of extracellular fields' base frequency by speed,

$$\nu_\theta = \nu_{\theta,0} + \beta \cdot s(t) \cdot \cos(\phi(t)), \tag{5}$$

was hypothesized by J. O'Keefe and M. Recce 30 years ago, upon discovery of coupling between θ-phase shift, $\phi(t)$, and spiking probability [48]. This dependence was thenceforth used in oscillatory interference models for explaining the hippocampal place cell [48, 49] and the entorhinal grid cell [50–52] firing. Several *in vitro* experiments [53–55] and Fourier-based LFP analyses [56] provide supporting evidence for these models (see however [57]). Here we find that θ-oscillons' dynamics, obtained directly from *in vivo* electrophysiological data conform with the previous studies. However, the hypothesized proportionality between the θ-frequency and speed is approximate—the actual dependence (4) may deviate from strict linearity. Second, the frequency expansion (3) may contain several oscillatory, speed-modulated terms, whereas the model expansion (5) contains only one (Fig. S6). Third, the modulation parameters are particularized, i.e., peak- and time-specific, albeit distributed around well-defined means. Thus, the θ-oscillons' structure fleshes out many details and exhibits the actual, empirical properties of speed-controlled oscillators driving the spectral wave (Fig. 4B,C,D). Note here that applying W-spectrogram analyses to the instantaneous Fourier frequencies do not capture any of these structures—the detailed spectral dynamics is averaged out (Fig. S7).

Noise. The qualitative difference between the regular and the irregular frequencies allows delineating the LFP's noise component. While in most empirical studies "noise" is identified *ad hoc*, as a cumulation of irregular fluctuations or unpredictable interferences within the signal [58–62], here noise is defined conceptually, based on intrinsic properties of Padé approximants to the signal's z-transform that are mathematically tied to stochasticity (Sec. VI B, [8–10]). Being that noise

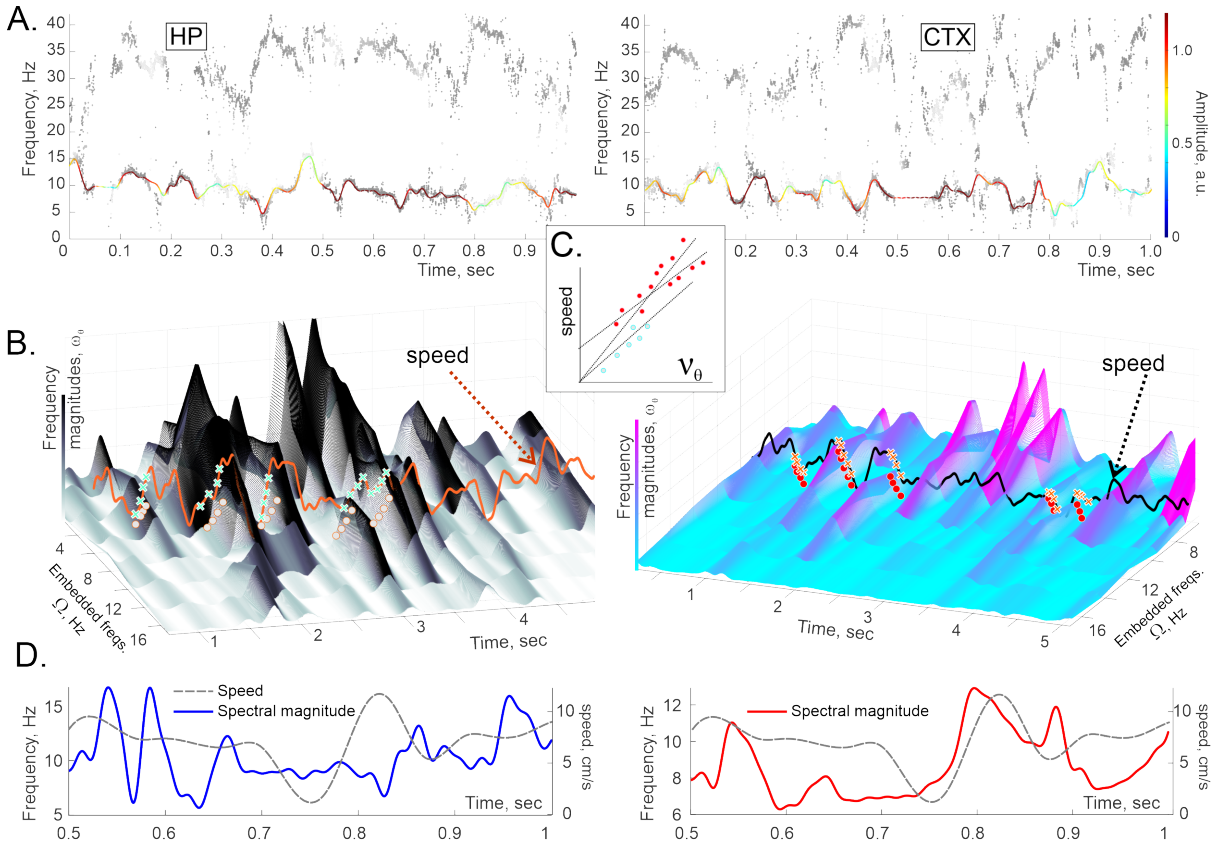

FIG. 4. **Spectral waves and embedded frequencies**. **A**. The spectral patterns produced via shifting-window evaluation of instantaneous frequencies are intermittent (Fig. 3A). To recapture the underlying continuous spectral dynamics, we interpolated the raw datapoints over a uniform time series, thus recovering the hippocampal (left) and the cortical (right) spectral waves with uninterrupted shapes. **B**. The contiguous data series allow constructing 3*D* Welch's spectrogram on which each peak along the frequency axis highlights a particular embedded frequency. Altitudinal shadowing emphasizes higher peaks (colorbar along the vertical axis). Note that most peaks in both hippocampal (left) and the cortical (right) *W*-spectrograms are localized not only in frequency but also in time, indicating short-lived perturbations of spectra. The dynamics of these frequencies is coupled with the speed—higher speeds drive up the magnitudes of the embedded frequencies. The speed profile is scaled vertically and shifted horizontally to best match the frequency magnitudes (orange and black trace respectively). While the response of the hippocampal frequency to speed is nearly immediate (about $\tau = 70 - 120$ ms delay), the cortical response is delayed by about $\tau = 300 \pm 50$ ms. **C**. Examples of the individual cortical peaks' magnitudes, sampled at random, over particular frequencies (heights of the dots on the panels B) and the corresponding speeds (heights of the crosses) exhibit clear quasi-linear dependencies. The exponents of these dependencies may slightly change from one appearance of a peak (an instantiation of an embedded frequency) to another. **D**. The net magnitude of the spectral wave (θ-bandwidth) co-varies with the speed with the delay of $\tau = 100$ ms, depending on the case, in the hippocampus (left panel) and an extra $\tau = 300$ ms in the cortex (right panel).

is qualitatively distinct from the oscillatory part, its dynamics provides complementary description of the network's state.

As indicated on Fig. 1C, in a typical LFP, only a few percent of the frequencies exhibit regular behavior, and yet their combined contribution is dominant: the stochastic component, $\xi(t)$, usually accounts for less than 5% of the signal's amplitude, i.e., the noise level is generally low [11, 12]. Structurally, the DPT noise component has undulatory appearance and can make positive or nega-

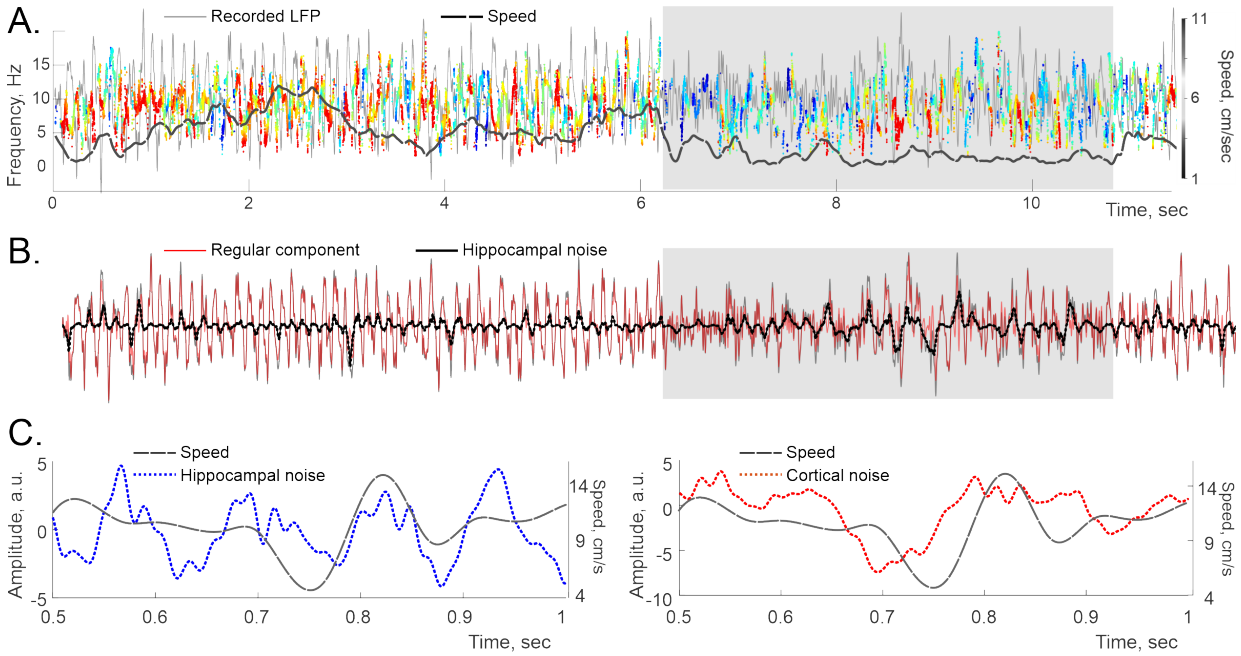

FIG. 5. **Spectral wave magnitude, noise and speed**. **A**. A segment of a hippocampal spectral wave shows magnitude increase during activity with speed, which reflects increased level of synchronization (see below). Shaded area highlights a period of slow motion, during which the noise escalates. The original LFP amplitude is shown by the gray trace in the background, for reference. The dashed black curve shows the animal's speed. **B**. The dynamics of the regular part of the LFP (red trace) and the noise component (dotted black trace), obtained for a 12-second lap. Original LFP is shown by gray trace in the background. **C**. The hippocampal (left panel) and cortical (right panel) noise levels follow speed, but more loosely than the oscillon's amplitude.

tive contributions to the net signal, modulated by the rat's physiological state [11, 12, 66], Fig. 5A, B. First, the noise amplitude tends to grow with speed (Fig. 5C), which suggests that increase of stochasticity is associated with the surge of the modulating vibrations (Fig. 4). However, the speed couples to noise weaker than to the oscillatory θ-amplitude or to the spectral wave (cortical separation $D(\xi^c, s) = 12.2 \pm 2\%$, hippocampal $D(\xi^h, s) = 10.6 \pm 1.5\%$, Fig. 4D). Yet, both hippocampal and cortical noise levels exhibit affinity, $D(\xi^h, \xi^c) \approx 14 \pm 2\%$. Most strongly, the noise is coupled to the amplitude of the oscillon that it envelopes, $D(\vartheta^h_\theta, \xi^h) = 1.2 \pm 0.5\%$, $D(\vartheta^c_\theta, \xi^c) = 1.5 \pm 0.5\%$, i.e., noise grows and subdues with the ups and downs of the physical amplitude of the extracellular field (Fig. 5B). As the animal moves out of the θ-state, noise amplifies by an order of magnitude and decouples from the locomotion, indicating an onset of a "non-theta" state [67], in which the amplitude of θ-oscillon drops by about $50 - 80\%$ (Fig. 5B, see also [68]).

IV. KURAMOTO OSCILLON

What is the genesis of the oscillons? It is commonly believed that the rhythmic LFP oscillations emerge from spontaneous synchronization of neuronal activity, although the specifics of these processes remain unknown [19–23]. A comprehensive analysis of the recorded data or modeling at the physiological level of detail is prohibitively complex and technically out of reach. Nevertheless, the essence of synchronization can be illustrated with simple computational models, which helps clarifying the observed phenomena. Specifically, the celebrated Kuramoto model allows tracing

the onset of synchronization in a population of oscillating units, using a single parameter that describes the coupling strength [69, 70]. Under fairly generic assumptions, these oscillators, or *phasors*, can qualitatively represent (map to) the recurring activity of individual neurons [73–77], so that their net population dynamics captures the ebb and flow of the mean extracellular field.

The behavior of each unit is described by a time-dependent phase, $\varphi_m(t)$, that changes between 0 and 2π, inducing an oscillatory output, $\ell_m = a_m\, e^{i\varphi_m}$. The field produced by the population of M phasors is hence

$$\sum_{m=1}^{M} a_m e^{i\varphi_m(t)} = A_K(t) e^{i\phi_K(t)}, \tag{6}$$

where $A_K(t)$ is the total amplitude and $\phi_K(t)$ the net phase. Each individual phase is coupled to the mean phase through an equation

$$\dot{\varphi}_m = 2\pi\nu_m + \lambda A_K \sin(\phi_K - \varphi_m), \tag{7}$$

where the dot denotes the time derivative and the constant λ controls the coupling. More extended discussions can be found in [69, 70], but in brief, such system can transition between two phases of behavior. For small couplings, different phases evolve nearly independently, proportionally to their proper angular speeds, $\varphi_m \approx 2\pi\nu_m t$. If these speeds are sufficiently dispersed, the phases remain out of sync and the net field remains small and irregular, $A_K(t) \approx 0$. As the coupling increases, the phases become more correlated. If the underlying frequencies are distributed close to a certain ensemble mean, $\bar{\omega}_m = \omega$, then the synchronized amplitude grows and regularizes with rising λ, and eventually produce a synchronous beat with the frequency ω.

From perspective of this discussion, this phenomenon is of interest because it may yield a solitary "synthetic" oscillon, that helps illustrating properties of the physiological oscillons. As shown on Fig. 6A, if the phasors' proper frequencies are distributed closely (within about ±3 Hz) to the mean frequency of $\nu_{\theta,0} \approx 8$ Hz, then the net field's dynamics is characterized by a single spectral wave that changes its properties according to the synchronization level. For weak couplings (small λs), synchronization is fragmentary: segments with steady frequency extend over a few oscillations, outside of which the spectral wave has a large magnitude (note that the oscillon's amplitude, A_K, remains low) and is carried by many embedded frequencies, as indicated by abundance of transient peaks on W-spectrograms (Fig. 6A, right panel). As λ grows, the net amplitude, A_K, increases and the segments of synchronicity lengthen, while the embedded oscillations subdue (Fig. 6B). As λ grows further, the embedded frequencies reduce in number and loose magnitudes, notably over the periods of increased synchronicity. As λ gets even higher, the oscillon turns into a simple harmonic, and its spectral wave degenerates into a line (Fig. 6C). Ultimately, spectral undulations get suppressed, as synchronization becomes fully dominant.

These observations suggest that the spectral wave's width (frequency deviation from the mean, $\Delta_\theta(t) = \nu_\theta(t) - \nu_{\theta,0}(t)$), may serve as an indicator of the ongoing synchronization level. From this perspective, the fact that both hippocampal and cortical θ-spectral waves are generally wide (±4 Hz, see Figs. 3A,C, 4A), implies that the physiological synchronization level is fairly low.

Note that Kuramoto oscillons produced by weakly-coupled ensembles often exhibit brief periods of regularity, with reduced spectral undulations, usually accompanied by higher amplitudes (Fig. 6A,B). Similar effects are observed in the empirical, physiological oscillons, where higher-synchronicity episodes, lasting about 50−70 ms in cortex and 100−200 ms in the hippocampus favor steady moves. Conversely, intensification of spectral undulations—local desynchronization—tends to co-occur with slowdowns and speed-ups (Fig. 6D, see also [68]). Thus, the physiological oscillons' response to higher speed effectively corresponds to the increase of coupling λ.

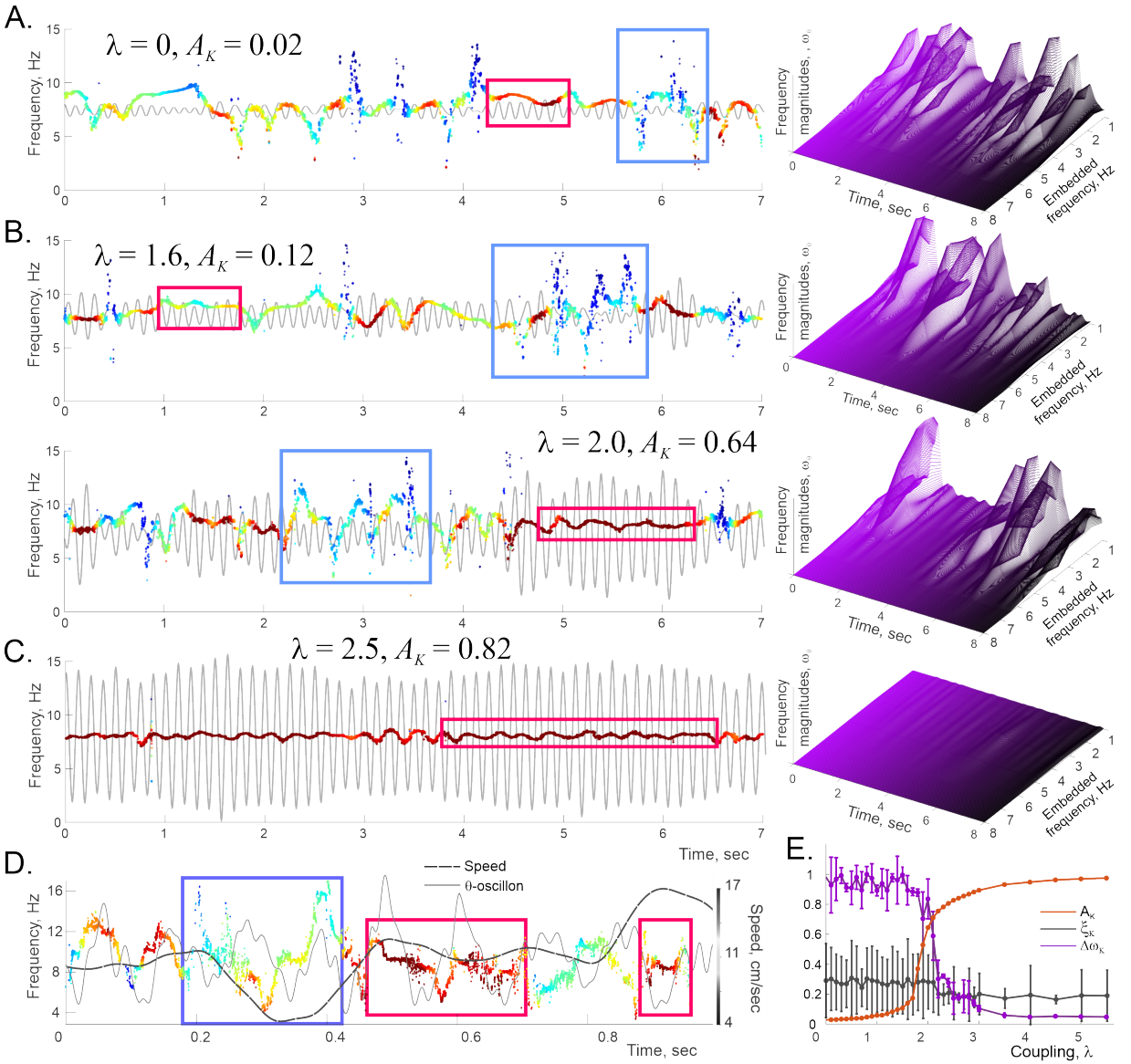

FIG. 6. **Kuramoto model**. 1000 oscillators (phasors) with base frequencies normally distributed around 8 Hz with the variance 1 Hz, coupled via equation 7, produce a mean field characterized by a single spectral wave—a solitary Kuramoto oscillon (gray trace in the background, scaled up on the top panel 10 times for visibility). On all panels, the maximal amplitude defines the color scale. **A**. At small couplings, K-oscillon has low amplitude ($A_K \lesssim 0.02A_{\max}$) and often reshapes (the spectral wave then disrupts, blue boxes). The W-spectrogram (right panel) shows that the embedded frequencies restructure at ~ 100 ms timescale. **B**. As the coupling between phasors grows, the synchronized amplitude builds up and the K-oscillon's shape regularizes. Note that when the spectral wave flattens out, the oscillon is nearly sinusoidal (strong synchronization, brown boxes), and the dynamics of the embedded frequencies during these periods are suppressed (right panel). **C**. At large couplings, synchronization becomes persistent: the spectral wave narrows, the embedded frequencies die out and the oscillon reduces to a nearly-sinusoidal harmonic. **D**. A hippocampal θ-oscillon regularizes its spectral wave and yields higher amplitude when the rat's speed is steady (gray dashed line, shifted by 80 ms); desynchronization occurs when the speed is low or transient. **E**. The oscillon's amplitude, A_K (orange curve), the magnitude of its spectral wave (purple curve), and the noise level, ξ (gray curve), for different coupling strengths. As the system synchronizes ($1.7 \lessapprox \lambda \lessapprox 3$), the amplitude grows, while the spectral undulations and the noise subdue. At higher couplings noise is suppressed and regular wave dominates.

Surprisingly, the Kuramoto model, being fully deterministic, also produces a noise component. At weak couplings, about 10% of the recovered frequencies are stable, while the other 90% exhibit erratic behavior and represent the *emerging* noise, ξ_K, which, however, is small and weakens with growing λ. Importantly, the distinction between noise and regularity is robust: injecting artificial noise, $\hat{\xi}$, white or colored, into the Kuramoto field, up to $\hat{\xi} \approx 10\xi_K$, does not alter the amplitude of the de-noised, regular Kuramoto oscillon. As shown on Fig. 6E, in the desynchronized state ($\lambda \lesssim 2$), the noise accounts for about 17% of the field, and then nearly disappears as the system synchronizes. In other words, high noise level may also be viewed as a signature of desynchronization, whereas regular oscillations dominate in synchronized states. This behavior is also in agreement with the physiological dynamics: as shown on Fig. 5, the noise level is lower during active moves, and heightened during quiescence, indicating that synchronization of the hippocampo-cortical network increases during the animal's activity [68].

V. DISCUSSION

The intricate structure of the synchronized extracellular fields can be anatomized using different decomposition techniques. The constituents brought forth by a particular decomposition provide a specific semantics for reasoning about the LFP functions. Being that these semantics may differ substantially, one may inquire which approach better reflects the physical structure of the brain rhythms. The oscillatory nature of LFPs suggests partitioning the signal into Fourier harmonics—an approach that dominates the field since the discovery of the brain waves [1–3]. However, its is also known that the Fourier techniques obscure the structure of noisy and nonstationary data—precisely the kind of signals that are relevant in biology [71]. In particular, these considerations apply to the LFPs, since their constituents—the oscillons—have transient structures enveloped by noise, i.e., are by nature noisy and nonstationary [11, 12].

Since the oscillons are constructed empirically, using a high time-frequency resolution technique, and exhibit stable, reproducible features that dovetail with theoretical models of synchronization, they likely capture the physical architecture of the extracellular fields, whereas the traditional, Fourier-defined brain waves provide approximative descriptions. Thus far, oscillons were observed in rodents' hippocampal and the cortical LFPs, but similar structure should be expected in generic brain rhythms. Their systematic analyses should help linking electrophysiological data to the synchronization mechanisms and reveal the dynamics of the noise component.

Lastly, the oscillons suggest a fresh vantage point for the principles of information transfer in the hippocampo-cortical network. Traditionally, the coupling of LFP rhythms to neuronal activity is traced through modulations of the brain waves' amplitudes and phases [31–37]. In contrast, frequency-modulated (FM) oscillons imply a complementary format, in which a slow-changing mean frequency defines the "channel of communication," over which the information is carried by the rapid phase and frequency alterations, reflecting fast endogenous dynamics and abrupt external inputs [12, 72]. In other words, Fourier analyses emphasize amplitude modulation (AM), while the DPT decomposition highlights the FM principles of information transfer, carried over several discrete channels [73–77]. In the case of θ-rhythms, the AM-format is manifested in familiar couplings of speed with the slowly changing mean frequencies, amplitudes, narrowing and widening of the θ-band, etc., whereas information about rapid activities appears to transmit across the hippocampo-cortical network via alterations of the embedded θ-frequencies.

Acknowledgments. The work was supported by NIH grants R01NS110806 (MZ and YD), R01AG074226 (NL and YD), R01DA054977 (CD and DJ) and NSF grant 1422438 (CH and YD).

VI. APPENDIX

A. Supplementary figures

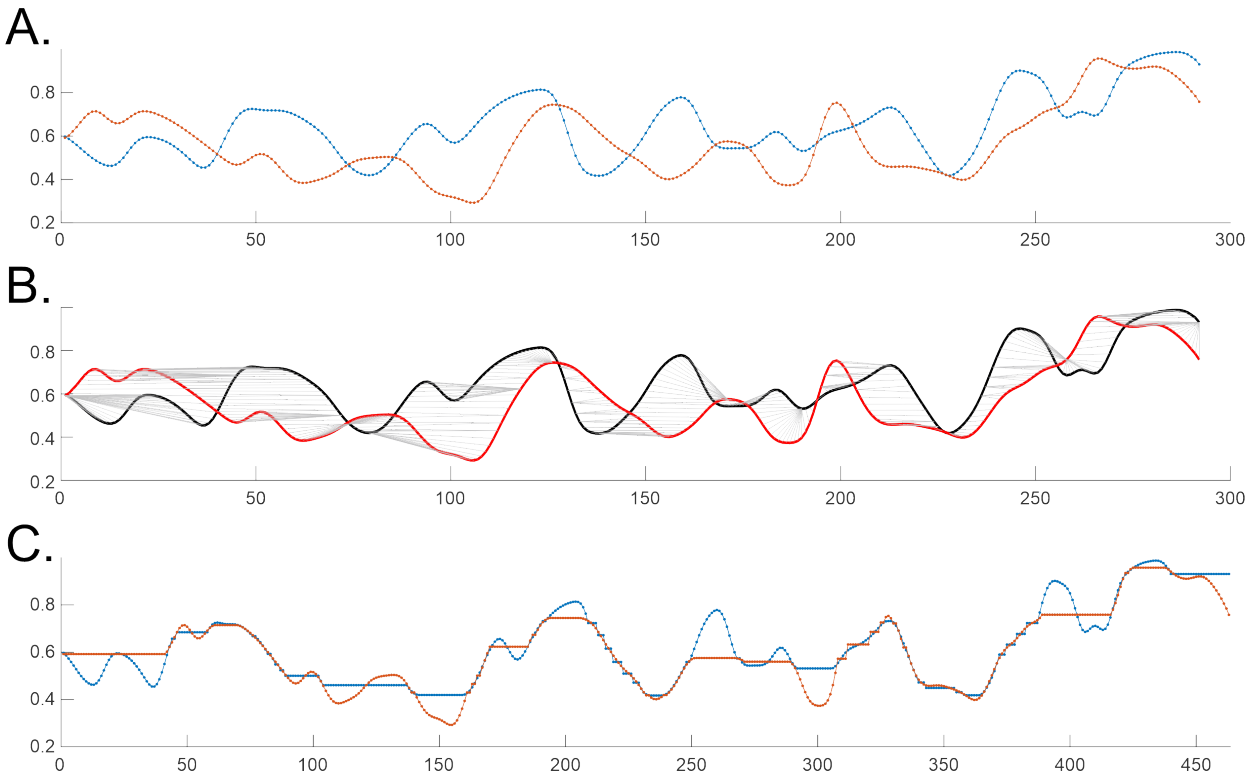

Fig. S1. **Dynamic Time Warping** (DTW) method is based on applying series of stretches that maximize alignment between two profiles at minimal cost, without omitting elements or scrambling their order. DTW is commonly used to quantify similarity between waveforms, e.g., for recognizing similar speech patterns [78], and is naturally suitable for comparing spectral waves. **A**. Two concurrent segments of the hippocampal, ν_θ^h (blue line), and the cortical, ν_θ^c (red line), spectral waves. Each segment contains about 300 data points (time-wise this amounts to about 40 ms), normalized by their respective means and shifted vertically into the $0 \lesssim y \lesssim 1$ range. **B**. Each point from ν_θ^h is matched to one or more points of ν_θ^c and vice versa, using MATLAB's dtw function. The gray lines show pairs of aligned points. One-to-many connection lines (gray) mark the stretchings. Note that different segments of spectral waves alternately lag and outpace one another: the algorithm compensates these shifts to match the shapes. **C**. After the alignments, the number of points increases by 50% (note the stretched-out x-axis). The point-by-point separation in the resulting alignment, measured in Euclidean metric and normalized to the original curve lengths serves quantifies the spectral waves' shape difference, which in this case amounts to 7%.

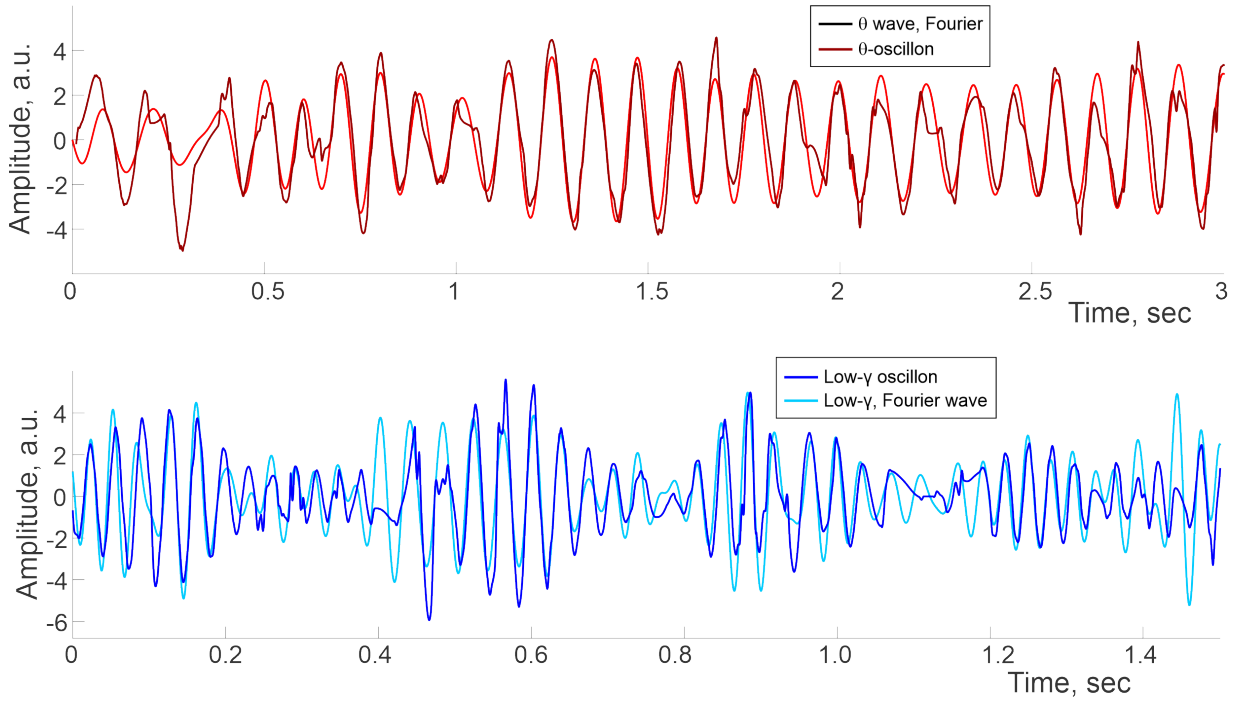

Fig. S2. **Comparative waveforms** of Fourier θ-wave ($4-12$ Hz) and θ-oscillon (top panel) and slow-γ wave, Fourier-filtered between 20 and 40 Hz, compared to slow-γ oscillon (bottom panel). Despite similar oscillation rates, the wave shapes are different.

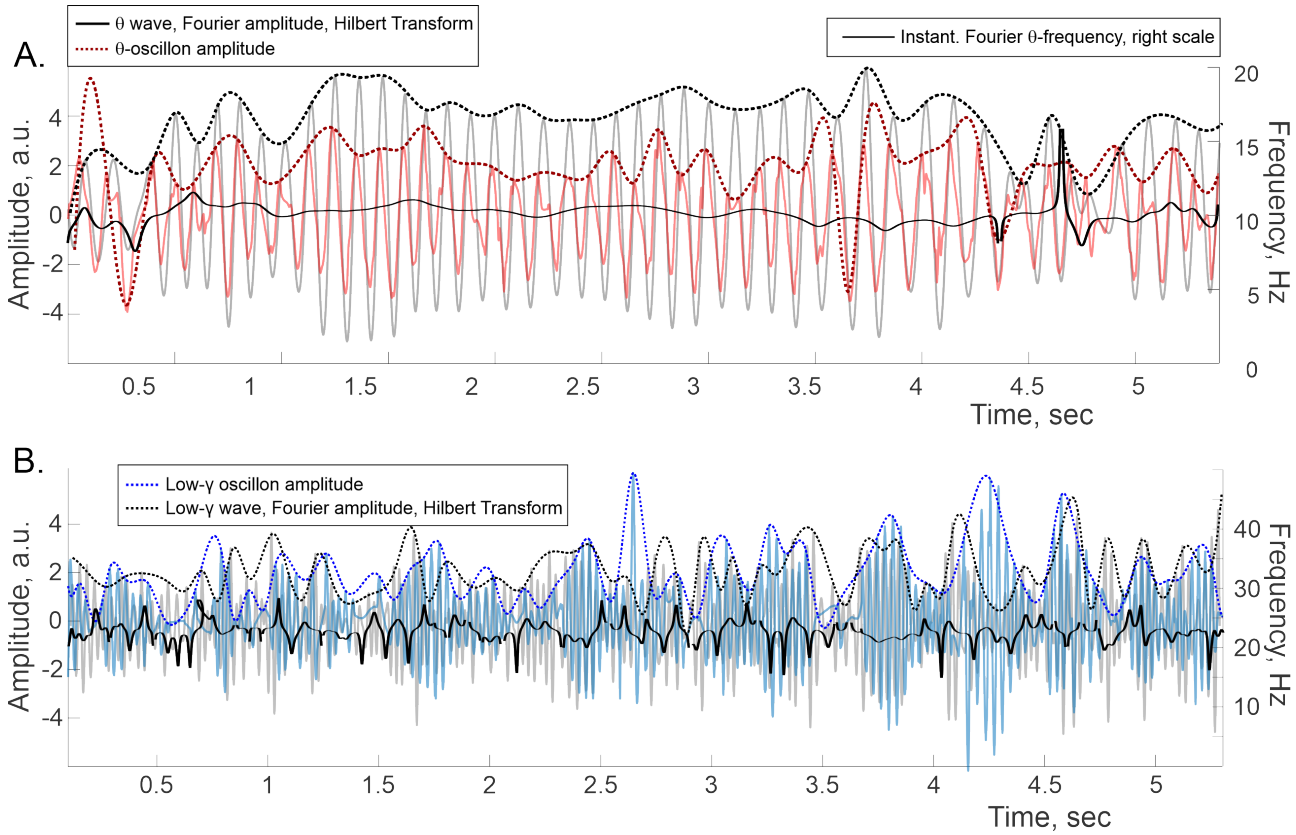

Fig. S3. **Hilbert transform**. **A**. Fourier-defined θ-wave (gray waveform in the background) shown with its amplitude (dotted line on top) and the corresponding instantaneous frequency (black line, placed according to the right scale) produced by Hilbert transform. Pink waveform in the foreground shows θ-oscillon and its amplitude computed from the net contribution of stable poles contributing to spectral wave (dotted brown line). **B**. Fourier-defined slow-γ wave (20 – 40 Hz), compared to the slow-γ oscillon. Amplitudes and frequencies are as above. The amplitude of the latter is lower because it does not include the noise component.

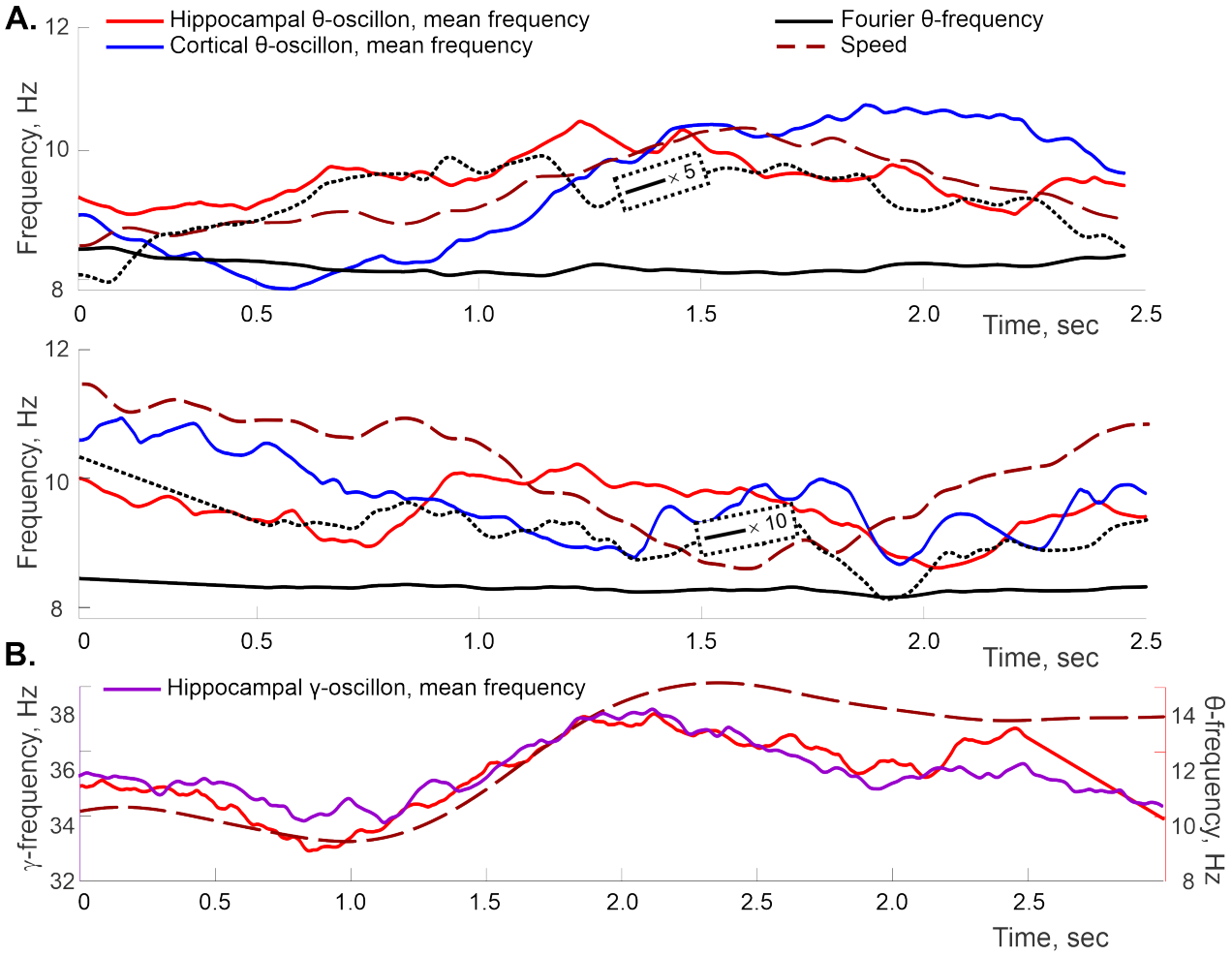

Fig. S4. **Speed vs. mean θ-frequency coupling**. **A**. Additional examples demonstrating covariance between the moving mean of the hippocampal (blue) and the cortical (red) θ-frequency with the rat's speed (dashed brown curve). The latter is scaled vertically and shifted as on Fig. 4, to match the frequency ranges. The instantaneous frequency of the traditional, Fourier-defined θ-waves is shown by solid black curve, as on Fig. 3. A five-fold (top panel) and ten-fold (bottom panel) vertical stretch of the Fourier-frequency produces the dotted black curve, whose similarity to the spectral waves' means explains the general correspondence between our results and conventional evaluations of speed-frequency couplings. **B**. Mean frequency profile of a hippocampal θ-oscillon, left-shifted by 300 ms (right scale), vs. the mean frequency of a hippocampal slow-γ oscillon, dark lilac, right-shifted by 500 ms (left scale), shown with the rat's speed profile.

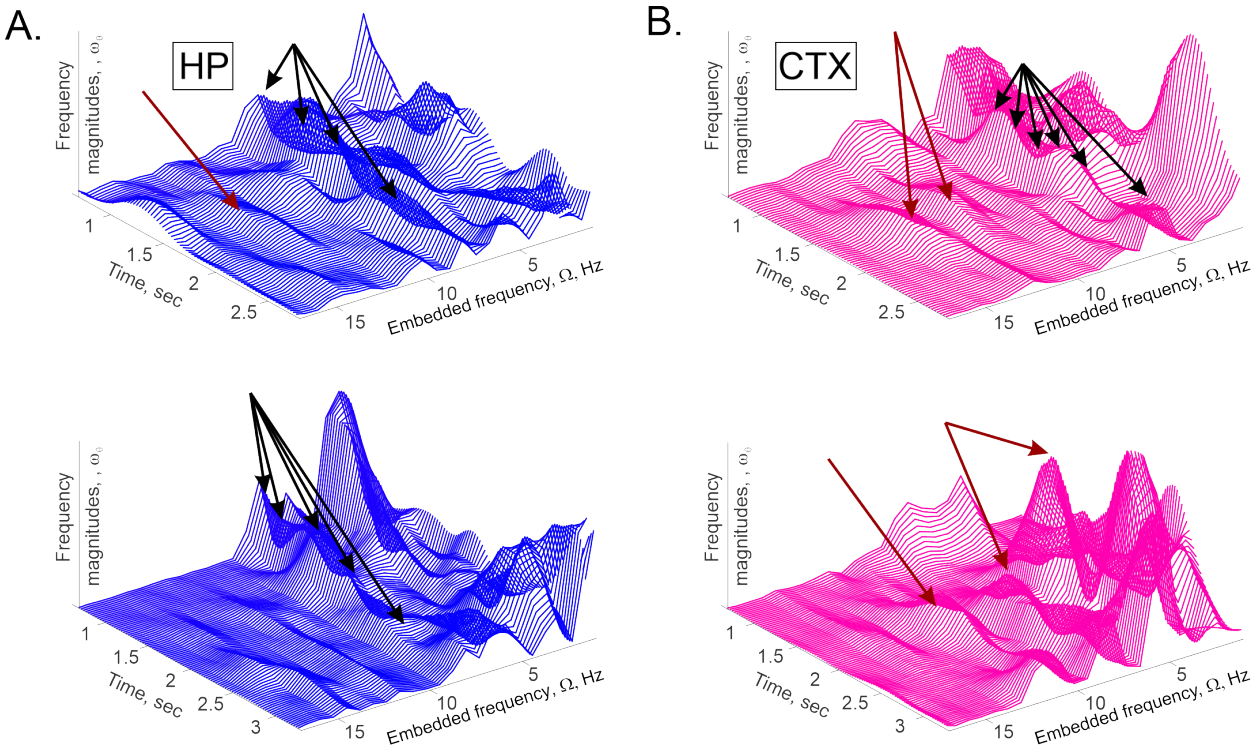

Fig. S5. **Additional examples** of hippocampal (left column) and cortical (right column) W-spectrograms, illustrating the embedded frequency dynamics for the θ-oscillons. Dark red arrows point at the appearances of isolated peaks and the black arrows point at the "seedbeds" of peaks recurring at the same frequency.

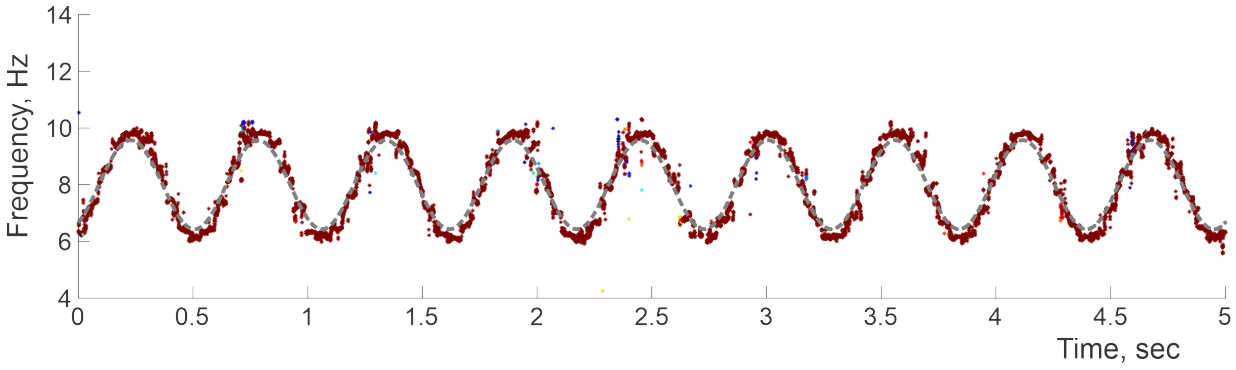

Fig. S6. **Solitary spectral wave**, used to simulate the oscillatory model (5) with a single modulating frequency, $\Omega_1/2\pi \approx 1.8$ Hz, oscillating around the mean $\nu_0 = 8$ Hz with the magnitude $\nu_1 \approx 2$ Hz (dashed gray line in the foreground). Dots represent the instantaneous DPT stable frequencies, colored according to their respective amplitudes. Physiological spectral waves shown on Figs 1 and 3 contain more than one frequency-modulating harmonic.

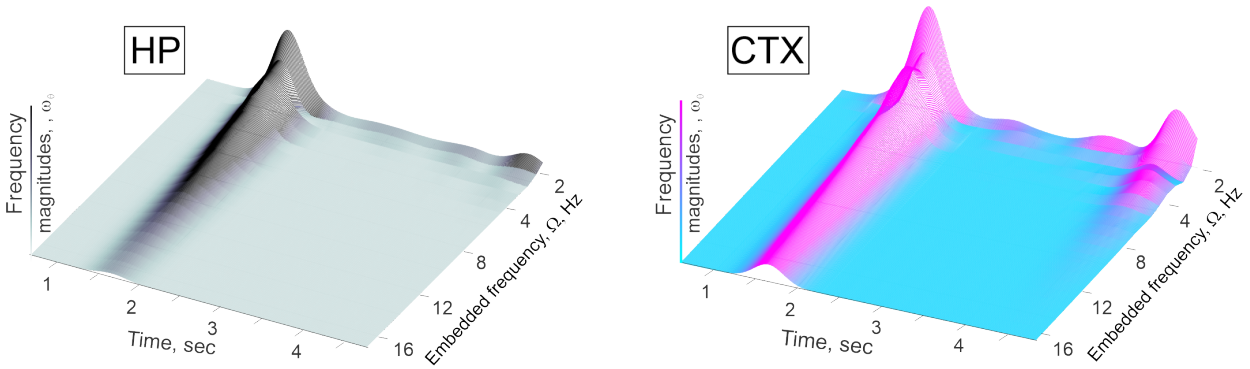

Fig. S7. **Welch spectrograms of Fourier instantaneous frequencies** (solid black line on the Fig. 3B) built for the hippocampal (left) and cortical (right) spectral-θ-waves, capture major frequency "splashes" at about 1.7 sec and 4.67 sec, but do not resolve rapid modulations of θ-frequency in-between, compare to Fig. S5.

B. Mathematical supplement

Fourier approach views signals as superpositions of harmonic waves. To evaluate their amplitudes, $2N$ data values, $\bar{\ell}_k = \{\ell_{k,1}, \ell_{k,2}, \ldots, \ell_{k,2N}\}$, centered around a discrete moment t_k, are convolved with a set of $2N$ discrete harmonics, $e^{i\pi/N}, e^{i2\pi/N}, e^{i3\pi/N}, \ldots, 1$,

$$A_{k,N} = \sum_{n=0}^{2N-1} \ell_{k,n} z_{2N}^{-n}, \tag{8}$$

where $z_{2N} = e^{i\pi/N}$. The longer is the sample set, the more precise is the spectral decomposition (8). Specifically, if the original signal is a superposition of N_P oscillators,

$$\ell(t) = \sum_{p=1}^{P} a_p e^{i2\pi(\nu_p t + \varphi_p)}, \tag{9}$$

with the amplitudes a_p, frequencies ν_p, and phases $2\pi\varphi_p$, sampled at discrete times $t_k = k\sigma$, then the Fourier amplitudes computed for a large number of data points are

$$A_{k,l} = \sum_k \ell(t_k) z_{2N}^{-k} = \sum_p \frac{a_p}{1 - z_l e^{i2\pi(\nu_p\sigma + \varphi_p)}} = \sum_p \frac{a_p}{1 - e^{i2\pi(\nu_p\sigma + \varphi_p - l/N)}}. \tag{10}$$

The closer a particular frequency $\nu_p\sigma + \varphi_p + i0$ is to a l/N, the higher is the amplitude $A_{k,l}$ of the corresponding harmonic. The segment selected for the analyses is then shifted, $\bar{\ell}_k \to \bar{\ell}_{k+1}$, yielding the next value of the amplitude, $A_{k+1,l}$, and so forth, over the entire signal span [80].

If the signal also contains noise,

$$\ell(t) = \sum_{p=1}^{P} a_p e^{i2\pi(\nu_p t + \varphi_p)} + \xi(t),$$

then the Fourier peaks broaden and their heights reduce [81]. Similar effects appear if the signal is nonstationary, e.g., if the frequencies ν_p change with time, since it becomes more difficult to match both the temporal and frequency details [7, 71, 79]. Indeed, resolving a spectral structure X that lasts over a period T_X, requires using time resolution, ΔT, shorter than T_X [6]. On the other hand, the frequency resolution, $\Delta\nu$, should be smaller than the X's spectral size. The problem is that improving the temporal resolution (lowering ΔT) reduces the number of data points caught into the sliding window, which then lowers the frequency resolution, $\Delta\nu = 1/\Delta T$, which limits the precision of the method altogether.

For example, the characteristic amplitude of the spectral waves shown on Fig. 1C and Fig. 3A is about $\Delta\nu \approx 7 - 12$ Hz, which, at the Nyquist frequency $S = 4$ kHz, requires at least $N = 600$ discrete harmonics, i.e., $N = 600$ data points per sliding window, that can be acquired over $\Delta T = N/S = 150$ ms. On the other hand, the characteristic period of the spectral waves is about $T_\theta \sim 50 - 100$ ms, i.e., in order to resolve the raising and the lowering phases of the spectral wave, ΔT should be less than 50 ms. Thus, the temporal and the frequency resolutions work against each other and leave certain details of X unresolved.

Discrete Padé Transform (DPT) approach is based on adapting the frequencies $\nu_1, \nu_2, \ldots, \nu_N$ according to the signal's structure, without restricting them to a regular "frequency grid" as in

(8) [8–10]. First, the discrete variable z_{2N} in (8) and (9) is replaced with a generic, continuous complex variable z, thus turning the sum (9) into a z-transform of the data series,

$$S(z) = \sum_{n=1}^{\infty} s_n z^{-n}. \tag{11}$$

The function (11) is then approximated by a ratio of two polynomials,

$$S_N(z) = P_{N-1}(z)/Q_N(z),$$

which constitutes the N-th order Padé approximation, $S(z) = S_N(z) + o(z^{2N})$ [82] (hence the name of the method [11]). As shown in [8, 9], the poles of $S_N(z)$, i.e., the roots of $Q_N(z)$, capture the spectral structure of the signal $\ell(t)$, similarly to the Fourier transform (10). Specifically, for the signal (9) one gets a rational function of degree $(N_P - 1)/N_P$,

$$S(z) = \sum_k s(t_k) z^k = \sum_p \frac{a_p e^{i\varphi_p}}{1 - z e^{i2\pi\nu_p\sigma}},$$

with the poles

$$z_p = e^{-i2\pi\nu_p\sigma},$$

and their residues defining the individual frequencies, ν_p, the amplitudes, a_p, and the phases, φ_p, of the corresponding oscillators.

If the signal contains a stochastic component $\xi(t)$, then the discretized time series are "noisy," $s_n = r_n + \xi_n$, and the generating function $S(z)$ acquires an "irregular" part

$$\Xi(z) = \sum_{n=0}^{\infty} \xi_n z^{-n}.$$

As it turns out, the poles of the Padé approximant to $\Xi(z)$ concentrate around the unit circle in the complex plane [63] and pair up with its roots, forming the so-called Froissart doublets [64, 65, 83, 84]. A typical pole-zero distance in the complex plane is smaller than $10^{-6} - 10^{-7}$ in the standard Euclidean metric, which allows detecting the Froissart doublets numerically. Additionally, these doublets are highly sensitive to the parameter changes, e.g., to sliding window size, whereas the unpaired poles of (10) remain stable and isolated. These differences allow delineating the LFP's noise component from the oscillations encoded by the stable poles [8, 9].

Data analyses. The mean amplitudes of the LFP time series was normalized to $\bar{\ell}(t) = 2$, with small amount of noise, $\delta\xi \approx 0.01\%$ of the total amplitude, added for numerical stability. The signal was then filtered into $1 \le f \le 60$ Hz band. The original sampling rate, $S = 8$ kHz, was interpolated to 36 kHz to improve the low-frequency spectral wave reconstruction. We then produced $2 - 3$ times undersampled sub-series, which were used for independent estimations of the regular frequencies. The sliding window width varied between $n_\varpi = 100$ to $n_\varpi = 200$ (for each undersampled subseries), which yields Padé approximants of orders $N = 50 - 200$. At the interpolated frequency, this corresponds to $T_\varpi = 8$ ms to $T_\varpi = 50$ ms time windows. To ensure maximal contiguity of the spectral waves, windows were shifted by one data point. These results remain stable under parameter variations, e.g., changes of the sliding window width [11]. The unstable frequencies were identified by detecting the Froissart doublets, with the critical pole-zero distance $d_F = 10^{-6}$ [8–11].

Welch transform allows estimating power spectra in transient signals [45]. Standard power spectra are evaluated by performing the discrete Fourier transform of the entire signal and computing the squared magnitude of the result. In Welch's approach, the signal is first split into a large number of highly overlapping shorter segments, and then the power spectrum of each segment is evaluated independently.

The power peaks obtained from a particular data segment thus mark the most prominent frequencies appearing over the corresponding time interval. Arranging such power profiles next to each other in natural order, one gets three-dimensional W-spectrograms illustrated on Fig. S8. By construction, the lateral sections of W-spectrograms are the instantaneous power—frequency profiles, whereas the longitudinal sections show the peaks' dynamics, that highlight the evolution of the corresponding embedded frequencies, $\Omega_{\theta,i}$.

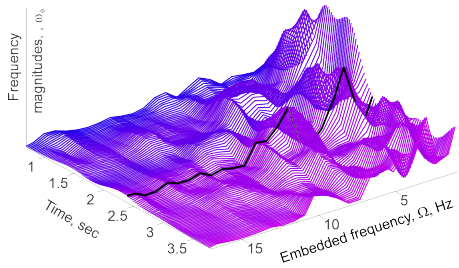

Fig. S8. **Welch spectrogram** of a hippocampal spectral wave. The black line shows power profile computed for a particular 600 ms long segment, centered at 2.4 sec. The select profile shows two peaks, which, over time, change their heights and positions, revealing the dynamic frequency landscape.

Spectral waves. Since the poles are computed independently at each time step, based on a finite number of data points, the patterns of reconstructed frequencies contain gaps and irregularities. To capture the underlying continuous physical processes, we interpolated the "raw" spectral traces over uniformly spaced time points and used Welch transform to analyze the embedded frequencies. The mean frequency was evaluated as the spectral waves' moving mean, over periods comparable with largest undulation span ~ 200 ms. All computations were performed in MATLAB.

Coupling between speed and the embedded frequencies (the dependence (4)) was obtained by evaluating the height of peaks on W-spectrogram at consecutive moments of time and comparing them to the ongoing speed values. Computations were made for peaks exceeding 20% of the mean height of W-spectrograms, for each analyzed data segment. All computations were performed in MATLAB.

Kuramoto model describes a network of oscillators, coupled via the equation

$$\dot{\varphi}_k = 2\pi\nu_k + \frac{\lambda}{m_k}\sum_{l=1}^{N} C_{kl}\sin\left(\varphi_l - \varphi_k\right),$$

where m_k is the valency of the oscillator ℓ_k, and C_{kl} is the adjacency matrix

$$C_{kl} = \begin{cases} 1 \text{ if } \ell_k \text{ is connected to } \ell_l, \\ 0 \text{ otherwise,} \end{cases}$$

and m_k is the valency of the node ℓ_k. In this study, the network had scale-free connectivity. The mean field produced at the k^{th} node is

$$A_{K,k}e^{i\phi_K} = \sum_{l=1}^{N} C_{kl}e^{i\varphi_l}. \tag{12}$$

Multiplying both sides of (12) by $e^{-i\varphi_k}$ and taking the imaginary part, one recovers the equation (7), which highlights the mean field dynamics.

VII. REFERENCES

[1] Buzsáki, G., Anastassiou, C. & Koch, C. The origin of extracellular fields and currents—EEG, ECoG, LFP and spikes. *Nat. Rev. Neurosci.* **13**: 407-402 (2012).

[2] Buzsáki, G. *Rhythms in the brain*. Oxford University Press, USA, (2011).

[3] Colgin, L. Rhythms of the hippocampal network. *Nat. Rev. Neurosci*. **17**: 239-249 (2016).

[4] Thut, G. Miniussi, C. & Gross, J. The Functional Importance of Rhythmic Activity in the Brain. *Current Biology* **22**: R658 (2012).

[5] Kopell, N., Kramer, M., Malerba, P. & Whittington, M. Are different rhythms good for different functions? *Front. Human Neurosci.*, **4**: 187 (2010).

[6] Brigham, E. *The fast Fourier transform and its applications*. Prentice Hall, Englewood Cliffs, N.J. (1988).

[7] van Vugt, M., Sederberg, P. & Kahana, M. Comparison of spectral analysis methods for characterizing brain oscillations. *J. Neurosci. Methods* **162**: 49 (2007).

[8] Bessis, D. Padé approximations in noise filtering. *J. Comput. & App. Math*. **66**(1-2): 85-88(1996).

[9] Bessis, D. & Perotti, L. Universal analytic properties of noise: introducing the J-matrix formalism. *J. Phys. A* **42**: 365202 (2009).

[10] Perotti, L. Vrinceanu, D. & Bessis, D. Enhanced Frequency Resolution in Data Analysis. *Amer. J. Comput. Math*. **3**, 242 (2013).

[11] Perotti, L., DeVito, J., Bessis, D. & Dabaghian, Y. Discrete spectra of brain rhythms, *Scientific Reports* **9**: 1105 (2019).

[12] Zobaer, M. S., Domenico, C., Perotti, L., Ji, D., & Dabaghian, Y. Rapid Spectral Dynamics in Hippocampal Oscillons. *Front. Comput. Neurosci.*, **16**: 880742 (2022).

[13] Jung, R. & Kornmüller, A. Eine methodik der ableitung lokalisierter potential schwankingen aus subcorticalen hirnyebieten. *Arch. Psychiat. Neruenkr*. **109**, 1–30 (1938).

[14] Buzsáki, G. Theta oscillations in the hippocampus. *Neuron* **33**(3), 325-40 (2002).

[15] Burgess, N. & O'Keefe, J. The theta rhythm. *Hippocampus* **15**: 825-826 (2005).

[16] Buzsáki, G. Theta rhythm of navigation: link between path integration and landmark navigation, episodic and semantic memory. *Hippocampus* **15**: 827-840 (2005).

[17] Colgin, L. Mechanisms and Functions of Theta Rhythms. *Annu. Rev. Neurosci*. **36**: 295-312 (2013).

[18] Colgin, L. Do slow and fast gamma rhythms correspond to distinct functional states in the hippocampal network? *Brain research* **1621**: 309-315 (2015).

[19] Arenas, A., Dáz-Guilera, A., Kurths, J., Moreno, Y. & Zhou, C., Synchronization in complex networks. *Phys. Rep*. **469**: 93-153 (2008).

[20] Liao, X., Xia, Q., Qian, Y., Zhang, L., Hu, G., & Mi, Y. Pattern formation in oscillatory complex networks consisting of excitable nodes. *Phys. Rev. E* **83**: 056204 (2011).

[21] Mi, Y. Liao, X., Huang, X., Zhang, L., Gu, W., Hu, G., & Wu, S. Long-period rhythmic synchronous firing in a scale-free network. *Proc. Natl. Acad. Sci.* **110**: E4931-E4936 (2013).

[22] Restrepo, J., Ott, E. & Hunt, B. Onset of synchronization in large networks of coupled oscillators. *Phys. Rev. E* **71**: 036151 (2005).

[23] Burton, S., Ermentrout, G. & Urban, N. Intrinsic heterogeneity in oscillatory dynamics limits correlation-induced neural synchronization. *J Neurophysiol*. **108** (2012).

[24] Domenico, C., Haggerty, D., Mou, X., & Ji, D. LSD degrades hippocampal spatial representations and

suppresses hippocampal-visual cortical interactions. *Cell reports*, **36**(11): 109714 (2021).

[25] Brandon, M., Bogaard, A., Schultheiss, N. & Hasselmo, M. Segregation of cortical head direction cell assemblies on alternating theta cycles. *Nat. Neurosci.*, **16**:739 (2013).

[26] Huxter, J., Senior, T., Allen, K. & Csicsvari, J. Theta phase-specific codes for two-dimensional position, trajectory and heading in the hippocampus. *Nat. Neurosci.* **11**: 587-594 (2008).

[27] Mizuseki, K., Sirota, A., Pastalkova, E. & Buzsáki, G. Theta oscillations provide temporal windows for local circuit computation in the entorhinal-hippocampal loop, *Neuron*, **64**: 267-280 (2009).

[28] Harris, K., Henze, D., Hirase, H., Leinekugel, X., Dagoi, G., Czurkó, A. & Buzsáki G. Spike train dynamics predicts theta-related phase precession in hippocampal pyramidal cells. *Nature* **417**: 738-741 (2002).

[29] Jezek, K., Henriksen, E., Treves, A., Moser, E. & Moser, M.-B. Theta-paced flickering between place-cell maps in the hippocampus. *Nature* **478**: 246-249 (2011).

[30] Brun, V., Solstad, T., Kjelstrup, K., Fyhn, M., Witter, M., Moser, E. & Moser, M-B. Progressive increase in grid scale from dorsal to ventral medial entorhinal cortex. *Hippocampus* **18**(12): 1200-12 (2008).

[31] Kennedy, J., Zhou, Y., Qin, Y., Lovett, S., Sheremet, A., Burke, S., & Maurer, A. A Direct Comparison of Theta Power and Frequency to Speed and Acceleration. *J. Neurosci*. **42**: 4326-4341 (2022).

[32] Kropff, E., Carmichael, J., Moser, E. & Moser, M.-B. Frequency of theta rhythm is controlled by acceleration, but not speed, in running rats. *Neuron*, **109**: 1-11 (2021).

[33] Richard, G., Titiz, A., Tyler, A., Holmes, G., Scott, R. & Lenck-Santini, P. Speed modulation of hippocampal theta frequency correlates with spatial memory performance. *Hippocampus*, **23**(12): 1269–1279 (2013).

[34] Young, C. K., Ruan, M., & McNaughton, N. Speed modulation of hippocampal theta frequency and amplitude predicts water maze learning. *Hippocampus*, **31**(2), 201–212 (2021).

[35] Chen, Z., Resnik, E., McFarland, J., Sakmann, B. & Mehta, M. Speed controls the amplitude and timing of the hippocampal gamma rhythm. *PloS one*, **6**(6), e21408 (2011).

[36] Ahmed, O. & Mehta, M. Running speed alters the frequency of hippocampal gamma oscillations. *J. Neurosci*. **32**(21): 7373–7383 (2012).

[37] Zheng, C., Bieri, K., Trettel S. & Colgin, L. The relationship between gamma frequency and running speed differs for slow and fast gamma rhythms in freely behaving rats. *Hippocampus* **25**(8): 924-938 (2015).

[38] Berndt, D. & Clifford, J. Using Dynamic Time Warping to Find Patterns in Time Series, Proceedings of the 3rd International Conference on Knowledge Discovery and Data Mining. AAAI Press: Seattle, WA. p. 359–370 (1994).

[39] Salvador, S. & Chan, P. Toward accurate dynamic time warping in linear time and space. *Intell. Data Anal*. **11**(5): 561–580 (2007).

[40] Neamtu, R., Ahsan, R., Rundensteiner, E., Sárközy, G., Keogh, E., Anh Dau, H., Nguyen, C. & Lovering, C. Generalized Dynamic Time Warping: Unleashing the Warping Power Hidden in Point-Wise Distances. Proceedings of 34th International Conference on Data Engineering (ICDE), pp. 521-532 (2018).

[41] Corduneanu, C. *Almost Periodic Oscillations and Waves*, Springer, New York (2009).

[42] Belluscio, M., Mizuseki, K., Schmidt, R., Kempter, R. & Buzsáki, G. Cross-frequency phase-phase coupling between theta and gamma oscillations in the hippocampus. *J. Neurosci*. **32**: 423-435 (2012).

[43] Shirvalkar, P., Rapp, P., & Shapiro, M. Bidirectional changes to hippocampal theta-gamma comodulation predict memory for recent spatial episodes. *Proc. Natl. Acad. Sci.* **107**(15): 7054–7059 (2010).

[44] Bullock, T., Buzsáki, G. & McClune, M. Coherence of compound field potentials reveals disconti-

nuities in the CA1-subiculum of the hippocampus in freely-moving rats. *Neuroscience* **38**: 609-619 (1990).

[45] Welch, P. The use of Fast Fourier Transform for the estimation of power spectra: A method based on time averaging over short, modified periodograms. *IEEE Trans. Audio & Electroacoustics*, **15**(2): 70–73 (1967).

[46] Proakis, J. & Manolakis, D. Digital Signal Processing: Principles, Algorithms and Applications, Upper Saddle River, NJ: Prentice-Hall (1996).

[47] Goutagny, R., Jackson, J. & Williams, S. Self-generated theta oscillations in the hippocampus. *Nat. Neurosci*., **12**(12): 1491–1493 (2009).

[48] O'Keefe, J. & Recce, M. Phase relationship between hippocampal place units and the EEG theta rhythm. *Hippocampus*, **3**(3): 317–330 (1993).

[49] Burgess, N. & O'Keefe, J. Models of place and grid cell firing and theta rhythmicity. *Curr. Opin. Neurobiol*., **21**(5): 734-44 (2011).

[50] Burgess, N., Barry, C.& O'Keefe, J. An oscillatory interference model of grid cell firing. *Hippocampus*, **17**(9): 801-12 (2007).

[51] Hasselmo, M., Giocomo, L. & Zilli, E. Grid cell firing may arise from interference of theta frequency membrane potential oscillations in single neurons. *Hippocampus*, **17**(12): 1252-71 (2007).

[52] Burgess, N., Grid cells and theta as oscillatory interference: Theory and predictions. *Hippocampus*, **18**(12): 1157-1174 (2008).

[53] Giocomo, L., Zilli, E., Fransén & Hasselmo, M. Temporal frequency of subthreshold oscillations scales with entorhinal grid cell field spacing. *Science* **315**(5819): 1719-22 (2007).

[54] Giocomo, L.& Hasselmo, M. Computation by oscillations: implications of experimental data for theoretical models of grid cells. *Hippocampus*, **18**(12): 1186-99 (2008).

[55] Shay, C., Boardman, I., James, N. & Hasselmo M. Voltage dependence of subthreshold resonance frequency in layer II of medial entorhinal cortex. *Hippocampus*. 22(8):1733-1749 (2012).

[56] Jeewajee, A., Barry. C., O'Keefe J. & Burgess N. Grid cells and theta as oscillatory interference: electrophysiological data from freely moving rats. *Hippocampus*, **18**(12): 1175-85 (2008).

[57] Domnisoru, C., Kinkhabwala, A. & Tank, D. Membrane potential dynamics of grid cells. *Nature* **495**: 199–204 (2013).

[58] Faisal, A., Selen, L. & Wolpert, D. Noise in the nervous system. *Nat. Rev. Neurosci.* 9, 292 (2008).

[59] Ermentrout, G., Galán, R., & Urban, N. Reliability, synchrony and noise. *Trends in neurosciences* 31, 428 (2008).

[60] Rowe, D., Nencka, A. & Hoffmann, R. Signal and noise of Fourier reconstructed fMRI data. *J. Neurosci Methods* **159**: 361-369 (2007).

[61] Stein, R., Gossen, E. & Jones, K. Neuronalvariability: noise or part of the signal? *Nat. Rev. Neurosci*. **6**: 389–397 (2005).

[62] McDonnell, M. & Ward, L. The benefits of noise in neural systems: bridging theory and experiment. *Nat. Rev. Neurosci*., **12**(7): 415–426 (2011).

[63] Steinhaus, H. Uber die Wahrscheinlichkeit dafuer dass der Konvergenzkreis einer Potenzreihe ihre natuerliche Grenze ist. *Mathematische Zeitschrift*, 408 (1929).

[64] Froissart, M. *Approximation de Padé: application á la physique des particules élémentaires*. CNRS, RCP, Programme n. 29, 1 (1969).

[65] Barone, P. A new transform for solving the noisy complex exponentials approximation problem. *J. Approx. Theory* **155**: 1 (2008).

[66] L. Perotti, T. Regimbau, D. Vrinceanu, D. Bessis, Identification of gravitational-wave bursts in high noise using Padé filtering. *Phys. Rev. D* **90**: 124047 (2014).

[67] Mysin, I. & Shubina, L. Hippocampal non-theta state: The "Janus face" of information processing. *Front Neural Circuits*. **17**:1134705 (2023).

[68] Hoffman, C., Cheng, J., Ji, D., & Dabaghian, Y. Pattern dynamics and stochasticity of the brain rhythms. *Proc Natl Acad Sci USA*. **120**(14): e2218245120 (2023).

[69] Kuramoto, Y. In H. Araki (ed.). Lecture Notes in Physics, Int. Symp Math. Problems Theor. Phys. Vol. 39. Springer-Verlag, New York. (1975).

[70] S. H. Strogatz, From Kuramoto to Crawford: exploring the onset of synchronization in populations of coupled oscillators. *Physica D* 143, 1 (2000).

[71] Grünbaum, F. The Heisenberg inequality for the discrete Fourier transform. *Applied and Computational Harmonic Analysis* **15**:163-167 (2003).

[72] Ziemer, R. & Tranter, W. *Principles of Communications: systems, modulation, and noise*. John Wiley & Sons Ltd, (2010).

[73] Izhikevich, E. Class 1 neural excitability, conventional synapses, weakly connected networks, and mathematical foundations of pulse-coupled models. *IEEE Trans. Neur. Netw*. **10**:499-507 (1999).

[74] Izhikevich, E. Weakly pulse-coupled oscillators, FM interactions, synchronization, and oscillatory associative memory. *IEEE Transactions on Neural Networks* **10**: 508-526 (1999).

[75] Hoppensteadt, F. & Izhikevich, E. Oscillatory Neurocomputers with Dynamic Connectivity. *Phys. Rev. Lett.* 82, 2983 (1999).

[76] Hoppensteadt, F. & Izhikevich, E. Thalamo-cortical interactions modeled by weakly connected oscillators: could the brain use FM radio principles? *Biosystems* **48**: 85-94 (1998).

[77] Hoppensteadt, F. & Izhikevich, E. *Weakly connected neural networks*. Springer, New York (1997).

[78] Sakoe, H. & Chiba, S. Dynamic programming algorithm optimization for spoken word recognition. *IEEE Transactions on Acoustics, Speech, and Signal Processing*. **26**(1): 43–49 (1978).

[79] Folland, G. & Sitaram, A. The uncertainty principle: A mathematical survey. *J. Fourier Anal. Applications* **3**: 207-238 (1997).

[80] Jacobsen, E. & Lyons, R. The sliding DFT. *Signal Processing Magazine, IEEE* **20**, 74 (2003).

[81] Newland, D. *An introduction to random vibrations, spectral and wavelet analysis*. Dover Publications, Mineola, N.Y. (2005).

[82] Baker G. & Graves-Morris, P., *Padé Approximants*. Cambridge Univ. Press, New York (1996).

[83] Gilewicz, J. & Pindor, M. Padé approximants and noise: A case of geometric series. *J. Comput. & Appl. Math*. **87**: 199-214 (1997).

[84] Gilewicz, J. & Kryakin, Y. Froissart doublets in Padé approximation in the case of polynomial noise. *J. Comput. & Appl. Math*. **153**: 235-242 (2003).